IEEE Access
Multidisciplinary | Rapid Review | Open Access Journal

Received October 11, 2021, accepted November 12, 2021, date of publication November 22, 2021,
date of current version December 27, 2021.

Digital Object Identifier 10.1109/ACCESS.2021.3129910

Optimal Coils and Control Matching in Wireless Power Transfer Dynamic Battery Chargers for Electric Vehicles

GIULIA DI CAPUA[1], (Senior Member, IEEE), AND NICOLA FEMIA[2], (Senior Member, IEEE)
[1]Department of Electrical and Information Engineering, University of Cassino and Southern Lazio, 03043 Cassino, Frosinone, Italy
[2]Department of Information and Electrical Engineering and Applied Mathematics, University of Salerno, 84084 Fisciano, Salerno, Italy

Corresponding author: Giulia Di Capua (giulia.dicapua@unicas.it)

This work was supported by the University of Salerno through the Project "Sistemi di Carica Induttiva di Veicoli Elettrici", under Grant 300638FRB18DICAPUA.

ABSTRACT Wireless Power Transfer (WPT) is a key enabling technology towards the transportation electrification, able to overcome some limits of the plug-in charging of the Electric Vehicle (EV). In this frame, a special attention is paid to the dynamic WPT systems, where the EV is recharged during motion. This paper presents a model and a resultant method for the system level design of a series-series WPT Dynamic Battery Charger (WPT-DBC) for EVs. The model allows analyzing the joined influence of coil pair characteristics and power converter stages controls on the global performances of WPT-DBCs. The design method provides general guidelines for system level optimization, matching the characteristics of the power and control elements of a series-series WPT-DBC, to achieve the desired efficiency, receiver power loss and battery charge.

INDEX TERMS Charge transfer maximization, dynamic battery charger, energetic efficiency, optimal control, wireless power transfer systems.

I. INTRODUCTION

The development of Wireless Power Transfer Dynamic Battery Chargers (WPT-DBC) for Electric Vehicles (EVs) has approached a quite good technological maturity level [1], [2]. Today several solutions implementing effective coil geometries and magnetic couplers, convenient power conversion architectures and control strategies are available [3]. A recent overview and comparative analysis on existing power conversion architectures and control methods in WPT-DBC for EVs is presented in [4]. Such a review paper discusses in details the typical magnetic couplers, the converter stages for the primary and the secondary side and the control handles associated with them, the compensation networks and their characteristics.

Fig. 1 shows the block diagram of a WPT charger, including transmitter (TX) and receiver (RX) coils and relevant power conversion stages. The coil pair characteristics, the compensation topology, the power conversion stages architecture and relevant controls, and the vehicle trajectory and speed determine the overall performances of a WPT charger.

The associate editor coordinating the review of this manuscript and approving it for publication was Qingchun Chen.

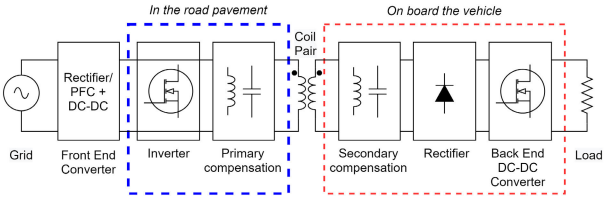

FIGURE 1. Block schematic of the different stages of a dynamic wireless power transfer system.

Normally, the development of a WPT charger starts from the coil pair design, based on given power ratings. Coil design constraints involve minimum efficiency requirements, safety issues relevant to the limitation of the leakage magnetic field, misalignment performance, cost, volume and weight. Some limitations on these issues are defined under standards like SAE J2954/1 [5] and IEC 61980-1:2015 [6]. Given the desired constraints to fulfill, the coil pair design process involves a series of steps, starting from practical choices (e.g., the minimum coupling to be ensured or the type of ferrite to be adopted), passing through the adoption of numerical and analytical modeling, to the final validation with the thermal modeling of the coil pair. In such a chain, the impact of compensation techniques cannot be neglected, and can be

studied by analyzing the input impedance seen by the power supply [7].

Recent progress in coil pair design for EVs are discussed in [8], where a summary on types, objectives, constraints, optimization algorithms and methodologies adopted for their design is provided, with a full discussion on the main coil structures properties (e.g., system complexity, misalignment tolerances, *etc.*). For example, in [9] unipolar and double D (DD) rectangular-shaped coils for wireless EV chargers are investigated. The coil pair sizes are designed to achieve the maximum coupling coefficient and efficiency. In [10] a new set of coil design formulas for high-efficiency and low harmonic currents with low magnetic field leakage for high-power WPT chargers is presented. Since the lower transfer efficiency is directly connected to low coupling coefficient, many efforts have been done in order to adapt the loosely coupled coil pair in WPT chargers. A bipolar DD coupler structure with a compensation-integrated feature is also proposed in [11], where an additional coil with smaller size is placed between the main TX coil and a ferrite layer for coupling enhancement. A novel array-type primary resonant coil design is proposed in [12], allowing to mitigate coil misalignments impact and improve the power transfer efficiency thanks to multiple independent TX coils, selectively powered based on their relative position with respect to the RX coil. Several optimization design processes have been proposed in the literature to support the optimal and innovative design of new coil pair structures, aiming to achieve maximization of the coil pair efficiency [13], power transfer capability [14], power density [15], weight and volume [16]. Enhanced evolutionary algorithms have been also proposed in the literature. An interesting advanced machine-learning algorithm has been applied to EV coil pair design to find a ferrite core structure with high magnetic coupling between the TX and RX coils [17]. Improved pad structures and a systematic design approach to achieve optimal primary DD pad have been also presented [18], based on a joint finite element method simulations and genetic algorithm.

Nowadays it is possible to design power stages with very high efficiency values, thus ensuring convenient power converters performances. In WPT static chargers it is also easy to set power converters control so as to achieve optimal performances within a given range of misalignment between the coils. However, in WPT-DBC additional goals must be accomplished, such as maintaining the power flow control regardless misalignment and velocity of the vehicles, and implementing segmentation control to energize the TX pad only when the vehicle is crossing it [19]. The simplest way to achieve these goals is based on controlling the power transfer on the transmitter side only, with a receiver side realized as a simple passive diode rectifier [20]–[22]. This simplifies the control, but limits the load (battery) regulation capability. Active receiver regulation makes the control more complex and may require additional sensors and communication between the primary and secondary sides [23], [24]. An effective WPT-DBC control is based on the impedance regulation on the receiver side, achieved by modulating the post-regulator duty-cycle so that the value of the equivalent load resistance at the rectifier output maximizes the power or efficiency rate. In [22], an optimal design against misalignment conditions in a Series–Series (SS) WPT-DBC is presented, providing optimal load matching thanks to a DC–DC converter, which guarantees the highest average transfer efficiency. In [25], a new charging technique, based on a sensorless identification of the actual presence of the vehicle over the receiver, realizes the load resistance matching to obtain the maximum power transfer in condition of nominal mutual coupling.

All cited prior studies are based on the use of nominal mutual coupling inductance for the WPT-DBC design. However, in WPT-DBC the mutual coupling inductance depends on the relative instantaneous positions of the TX-RX coils. Therefore, the magnetic coupling profile along the vehicle trajectory must be considered to achieve optimal performances. This is the real motivation of the WPT-DBC modeling and design discussed in this paper. In particular, we aim to achieve the system-level optimization of a WPT-DBC based on the optimal matching of coil pair mutual coupling profile and power conversion control setup. First, the paper provides the complete analytical model of coil pair and control system referring to a SS-WPT-DBC. Then, a novel system-level design approach is proposed, to effectively match coils characteristics and power electronics control setup on energy and efficiency performances. The proposed design approach is valid for any WPT-DBC architecture and is scalable, as the analysis and design equations are derived by using dimensionless factors, parameters and metrics.

The paper is organized as follows. In Section II, the unified analytical model of a SS-WPT-DBC is presented. In Section III, a method allowing the set-up of optimal inverter and post-regulator controls and mutual inductance profile is proposed. In Section IV, a real SS-WPT-DBC prototype is considered to validate the model and design method presented in the paper. The results of PSIM simulations confirm the theoretical model predictions. In Section V, conclusions are eventually drawn.

II. WPT-DBC ANALYSIS

The block schematic of a dynamic WPT system is shown in Fig. 1. The inverter stage – in its multiple configurations, e.g. voltage fed single-phase or multi-phase [26], [27], current fed push-pull [28], *etc.* – normally uses duty-cycle and/or phase-shift control actions, to realize the transmitter regulation. The receiver side is typically made of a full-bridge diode rectifier [20], followed by a DC-DC converter (buck, boost or buck-boost) with duty-cycle control, and a possible battery management system [29]. In this paper, the SS-WPT-DBC shown in Fig. 2 is considered as reference case study to illustrate the proposed system-level modeling and design approach for WPT-DBC systems. Nevertheless, with no loss

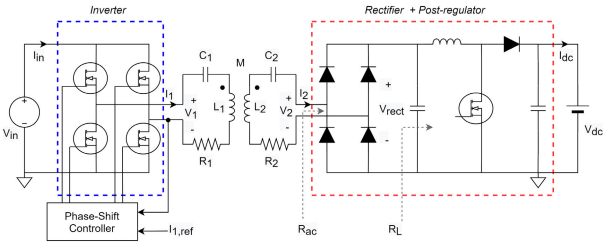

FIGURE 2. Series-series resonant wireless power transfer dynamic battery charger.

of generality, the same modeling and design approach can be applied to different compensation topologies and conversion architectures.

The SS-WPT-DBC of Fig. 2 is comprised of a Pulse-Width Modulated (PWM) inverter feeding the TX coil, a diode bridge rectifying the RX coil current, and a PWM DC-DC boost back-end converter. The coils and the resonant capacitors determine the TX and RX total resistances R_1 and R_2. At resonance, the First-Harmonic Approximation (FHA) model of the WPT system is given by (1):

$$\overline{V_1} = R_1\overline{I_1} - \mathrm{j}\omega_o M\overline{I_2} \tag{1.a}$$
$$\overline{V_2} = R_{ac}\overline{I_2} = \mathrm{j}\omega_o M\overline{I_1} - R_2\overline{I_2} \tag{1.b}$$

where $\bar{I}_1$ and $\bar{I}_2$ are the currents in the TX and in the RX, respectively, ω_o is the chosen resonance angular frequency, M is the mutual coupling, R_{ac}=V_2/I_2=$8\,R_L/\pi^2$ is the equivalent FHA resistance at rectifier input, and $R_L = V_{rect}/I_{rect}$ is the equivalent load resistance at the boost converter input [25]. Solving (1) yields the nominal amplitude of the currents on the two side of the system:

$$I_1 = \frac{4V_{in}}{\pi R_1}\left[\frac{n_i\,(1+r_{ac})}{1+m+r_{ac}}\right] \tag{2.a}$$
$$I_2 = \frac{4V_{in}}{\pi R_{12}}\left[\frac{n_i\sqrt{m}}{1+m+r_{ac}}\right] \tag{2.b}$$

where $R_{12} = \sqrt{R_1R_2}$ and the following dimensionless factors have been introduced:

$$m = \frac{\omega_o^2 M^2}{R_1R_2} \tag{3}$$
$$r_{ac} = \frac{R_{ac}}{R_2} = \frac{8V_{dc}}{\pi^2 R_2 I_{dc}}n_p^2 \tag{4}$$
$$n_i = \frac{\pi}{4}\frac{V_1}{V_{in}} = \sin\left(\frac{\pi}{2}D_i\right) \tag{5}$$
$$n_p = \frac{V_{rect}}{V_{dc}} = 1 - D_p \tag{6}$$

D_i and D_p being the PWM inverter and boost converter duty-cycles (see Fig. 2). From (2), the inverter input current and the load output current are then determined as given in (7.a) and (7.b). In addition, the current I_{dc} can also be obtained from (4), resulting in (7.c).

$$I_{in} = \frac{2}{\pi}n_iI_1 = \frac{8V_{in}}{\pi^2R_1}\left[\frac{n_i^2\,(1+r_{ac})}{1+m+r_{ac}}\right] \tag{7.a}$$
$$I_{dc} = \frac{2}{\pi}n_pI_2 = \frac{8V_{in}}{\pi^2R_{12}}\left[\frac{n_in_p\sqrt{m}}{1+m+r_{ac}}\right] \tag{7.b}$$
$$I_{dc} = \frac{8V_{dc}}{\pi^2 r_{ac}R_2}n_p^2 \tag{7.c}$$

Equations (7) highlight that the DC input and output currents I_{in} and I_{dc}, which determine the power rating and the efficiency of the WPT-BDC, depend on the dimensionless factors given in the square brackets. These factors are determined by the normalized squared mutual inductance m, the inverter and post-regulator conversion ratios n_i and n_p, and the normalized equivalent load resistance r_{ac} seen at the input of the rectifier stage. The vehicle trajectory and speed determine the mutual inductance time evolution $m\,(x_t,\ y_t)$, where $(x_t,\ y_t)$ are the coordinates at the time t of the trajectory of the RX coil mounted on-board the vehicle, moving with respect to the TX coil fixed to the ground.

The inverter and post-regulator converter duty-cycles are determined by the relevant controls, which are set to regulate the TX current at a given reference value $I_{1,ref}$, and the rectifier input resistance at a given reference value $r_{ac,ref}$. Accordingly, (7.a) and (7.c) can be solved for n_i and n_p (or equivalently, for D_i and D_p), yielding (8.a) and (8.b):

$$n_i = \frac{1+r_{ac,ref}+m}{v_{in}\left(1+r_{ac,ref}\right)} \tag{8.a}$$
$$n_p = \frac{r_{ac,ref}\sqrt{m}}{v_{dc}\left(1+r_{ac,ref}\right)} \tag{8.b}$$

where the coefficients v_{in} and v_{dc} are given in (9)

$$v_{in} = \frac{4V_{in}}{\pi R_1 I_{1,ref}} \tag{9.a}$$
$$v_{dc} = \frac{4V_{dc}}{\pi R_{12} I_{1,ref}} \tag{9.b}$$

The inverter and post-regulator converter duty-cycles must ensure $D_{i\min} \le D_i \le D_{i\max}$ and $D_{p\min} \le D_p \le D_{p\max}$. $D_{i\min}$ and $D_{i\max}$ are determined by the minimum ON time and OFF time of the inverter control, and by the dead time between the ON/OFF commutations of the two MOSFETs of each inverter leg. $D_{p\min}$ and $D_{p\max}$ are determined by the minimum ON time and OFF time of the post-regulator control. From (8), given V_{in}, V_{dc}, $I_{1,ref}$ and $r_{ac,ref}$, the inverter duty-cycle D_i and post-regulator duty-cycle D_p are subjected to the following conditions:

$$D_i = \begin{cases} D_{i\min} & m < m_{Di\min} \quad (10.a)\\ \dfrac{2}{\pi}\sin^{-1}\left[\dfrac{1+r_{ac,ref}+m}{v_{in}\left(1+r_{ac,ref}\right)}\right] & m_{Di\min} \le m \le m_{Di\max} \quad (10.b)\\ D_{i\max} & m > m_{Di\max} \quad (10.c)\end{cases}$$

$$D_p = \begin{cases} D_{p\max} & m < m_{Dp\min} \quad (11.a)\\ 1 - \dfrac{r_{ac,ref}\sqrt{m}}{v_{dc}\left(1+r_{ac,ref}\right)} & m_{Dp\min} \le m \le m_{Dp\max} \quad (11.b)\\ D_{p\min} & m > m_{Dp\max} \quad (11.c)\end{cases}$$

where

$$m_{Di\,\min} = \left(1 + r_{ac,ref}\right)\left(v_{in}\, n_{i\,\min} - 1\right) \tag{12.a}$$

$$m_{Di\,\max} = \left(1 + r_{ac,ref}\right)\left(v_{in}\, n_{i\,\max} - 1\right) \tag{12.b}$$

$$m_{Dp\,\min} = \left[\frac{v_{dc}\, n_{p\,\min}\left(1 + r_{ac,ref}\right)}{r_{ac,ref}}\right]^2 \tag{13.a}$$

$$m_{Dp\,\max} = \left[\frac{v_{dc}\, n_{p\,\max}\left(1 + r_{ac,ref}\right)}{r_{ac,ref}}\right]^2 \tag{13.b}$$

with $n_{i\min}$ and $n_{i\max}$ given by (5) for $D_i = D_{i\min}$ and $D_i = D_{i\max}$, and $n_{p\min}$ and $n_{p\max}$ given by (6) for $D_p = D_{p\max}$ and $D_p = D_{p\min}$, respectively. During the vehicle transit over the TX coil, the value of m varies from a minimum value (when the RX coil starts overlapping the TX coil) to a maximum value (named as peak value, m_{pk}), and returns to a minimum value again (when the RX coil ends overlapping the TX coil). In theory, according to (10)(11), there can be up to nine different possible operating conditions for the inverter and post-regulator converter stages, depending on the values of $m_{Di\min}$, $m_{Di\max}$, $m_{Dp\min}$ and $m_{Dp\max}$. In reality, some of these conditions never occur. In fact, the post-regulator can operate at the maximum value of the duty-cycle ($D_{p\max} \approx 1$) with consequent $m_{Dp\min} \approx 0$, according to (13.a). This condition allows an easier detection of the vehicle (RX coil) while approaching the TX coil, as shown in [25]. Moreover, the saturation down to $D_{p\min}$ of the post-regulator duty-cycle is quite unlikely, as $m_{Dp\max}$ is normally very high, according to (13.b). Therefore, it makes sense to consider the inverter duty-cycle saturation only, with the post-regulator duty-cycle D_p valid for $m_{Dp\min} \le m \le m_{Dp\max}$. Based on (7) and (10), we get:

$$I_{in} = \begin{cases} I_{in0}\dfrac{n_{i\,\min}^2 v_{in}\left(1 + r_{ac,ref}\right)}{\left(1 + m + r_{ac,ref}\right)} & m < m_{Di\,\min} \quad (14.a) \\ I_{in0}\dfrac{\left(1 + m + r_{ac,ref}\right)}{v_{in}\left(1 + r_{ac,ref}\right)} & m_{Di\,\min} \le m \le m_{Di\,\max} \quad (14.b) \\ I_{in0}\dfrac{n_{i\,\max}^2 v_{in}\left(1 + r_{ac,ref}\right)}{\left(1 + m + r_{ac,ref}\right)} & m > m_{Di\,\max} \quad (14.c) \end{cases}$$

$$I_{dc} = \begin{cases} I_{dc0}\dfrac{n_{i\,\min}^2 v_{in}^2 r_{ac,ref} m}{\left(1 + m + r_{ac,ref}\right)^2} & m < m_{Di\,\min} \quad (15.a) \\ I_{dc0}\dfrac{r_{ac,ref} m}{\left(1 + r_{ac,ref}\right)^2} & m_{Di\,\min} \le m \le m_{Di\,\max} \quad (15.b) \\ I_{dc0}\dfrac{n_{i\,\max}^2 v_{in}^2 r_{ac,ref} m}{\left(1 + m + r_{ac,ref}\right)^2} & m > m_{Di\,\max} \quad (15.c) \end{cases}$$

where

$$I_{in0} = \frac{2I_{1,ref}}{\pi} \tag{16.a}$$

$$I_{dc0} = \frac{R_1 I_{1,ref}^2}{2V_{dc}} \tag{16.b}$$

The post-regulator duty-cycle D_p expressions are given by:

$$D_p = \begin{cases} 1 - \dfrac{n_{i\,\min} v_{in}\, r_{ac,ref}\sqrt{m}}{v_{dc}\left(1 + m + r_{ac,ref}\right)} & m < m_{Di\,\min} \quad (17.a) \\ 1 - \dfrac{r_{ac,ref}\sqrt{m}}{v_{dc}\left(1 + r_{ac,ref}\right)} & m_{Di\,\min} \le m \le m_{Di\,\max} \quad (17.b) \\ 1 - \dfrac{n_{i\,\max} v_{in}\, r_{ac,ref}\sqrt{m}}{v_{dc}\left(1 + m + r_{ac,ref}\right)} & m > m_{Di\,\max} \quad (17.c) \end{cases}$$

where (17.a) and (17.c) are obtained from (7.c) by imposing $n_i = n_{i\min}$ and $n_i = n_{i\max}$, respectively.

The charge absorbed by the system and the charge delivered to the battery during the vehicle transition over the TX coils are given by (18) and (19):

$$Q_{in} = \int_{t_s}^{t_e} I_{in}(t)dt \tag{18}$$

$$Q_{dc} = \int_{t_s}^{t_e} I_{dc}(t)dt \tag{19}$$

where t_s and t_e represent the time instants when the RX coil starts and ends overlapping the TX coil (where $m \approx 0$), and $\Delta t = t_e - t_s$ is the time the RX coil takes to transit over a single TX coil at constant speed. During the interval $[t_s, t_e]$, we can identify a subinterval $[t_{Dimin}, t_{Dimax}]$, wherein $m_{Di\min} \le m \le m_{Di\max}$ (no inverter duty-cycle saturation), and two subintervals $[t_s, t_{Dimin}]$ and $[t_{Dimax}, t_e]$, wherein $m < m_{Di\min}$ and $m > m_{Di\max}$, respectively. From (14)(15) and (18)(19), we get:

$$Q_{in} = I_{in0}\left[\frac{\Delta t_0}{v_{in}} + \frac{\Gamma_{m0}}{v_{in}\left(1 + r_{ac,ref}\right)} + v_{in}\left(1 + r_{ac,ref}\right)\Gamma_{m1}\right] \tag{20.a}$$

$$Q_{dc} = I_{dc0} r_{ac,ref}\left[\frac{\Gamma_{m,0}}{\left(1 + r_{ac,ref}\right)^2} + v_{in}^2\Gamma_{m2}\right] \tag{20.b}$$

where the following integrals have been adopted:

$$\Gamma_{m0} = \int_{t_{Di\,\min}}^{t_{Di\,\max}} m\left(x_t, y_t\right) dt \tag{21.a}$$

$$\Gamma_{m1} = \int_{t_s}^{t_{Di\,\min}} \frac{n_{i\,\min}^2}{1 + m(x_t, y_t) + r_{ac,ref}} dt + \int_{t_{Di\,\max}}^{t_e} \frac{n_{i\,\max}^2}{1 + m(x_t, y_t) + r_{ac,ref}} dt \tag{21.b}$$

$$\Gamma_{m2} = \int_{t_s}^{t_{Di\,\min}} \frac{n_{i\,\min}^2\, m(x_t, y_t)}{\left[1 + m(x_t, y_t) + r_{ac,ref}\right]^2} dt + \int_{t_{Di\,\max}}^{t_e} \frac{n_{i\,\max}^2\, m(x_t, y_t)}{\left[1 + m(x_t, y_t) + r_{ac,ref}\right]^2} dt \tag{21.c}$$

Equations (20)(21) provide the basis to investigate two different kind of problems:

1) optimize the WPT-DBC performances, given the operating conditions and the mutual inductance;
2) optimize the mutual inductance, given the operating conditions and the required WPT-DBC performances.

Next Section discusses these design optimization goals.

III. WPTS DESIGN

A. INVERTER AND POST-REGULATOR OPTIMIZATION

Let us start by investigating the problem 1), by searching the values of $r_{ac,ref}$ and $I_{1,ref}$ that can optimize the charge and efficiency performances, given the operating conditions and the normalized squared mutual inductance. The first key point to be clarified is the impact of the inverter duty-cycle saturation, which involves the presence of the integrals Γ_{m1} and Γ_{m2} in (20). The values $m_{Di\min}$ and $m_{Di\max}$ that always allow to prevent the inverter duty-cycle saturation are given by (22):

$$m_{Di\,\min} \le 0 \Rightarrow\ D_{i\,\min} \le \frac{2}{\pi}\sin^{-1}\left(\frac{1}{v_{in}}\right) = D_0 \tag{22.a}$$

$$m_{Di\,\max} \ge m_{pk} \Rightarrow r_{ac,ref} \ge \frac{m_{pk}}{v_{in} n_{i\,\max} - 1} - 1 \tag{22.b}$$

Accordingly, if it is possible to set $m_{Di\min}$ and $m_{Di\max}$ so that the inverter duty-cycle never saturates, then from (20) we get:

$$Q_{in} = \Delta t_0 \frac{R_1 I_{1,ref}^2}{2\,V_{in}} \frac{1 + m_{av} + r_{ac,ref}}{1 + r_{ac,ref}} \tag{23.a}$$

$$Q_{dc} = \Delta t_0 \frac{R_1 I_{1,ref}^2}{2\,V_{dc}} \frac{m_{av} r_{ac,ref}}{\left(1 + r_{ac,ref}\right)^2} \tag{23.b}$$

where $m_{av} = \Gamma_{m0}/\Delta t_0$ is the average value of m over the vehicle trajectory. Consequently, (24) gives the resulting energy efficiency:

$$\eta = \frac{V_{dc} Q_{dc}}{V_{in} Q_{in}} = \frac{m_{av} r_{ac,ref}}{\left(1 + r_{ac,ref}\right)\left(1 + m_{av} + r_{ac,ref}\right)} \tag{24}$$

In (23)(24), the influence of m_{av} and $r_{ac,ref}$ is separated. This allows understanding their independent impact on the WPT-DBC performances. Evidently, both the charge delivered to the load and the energy efficiency increase if m_{av} increases. As for $r_{ac,ref}$, the charge delivered to the load decreases if $r_{ac,ref}$ increases for $r_{ac,ref} > 1$, whereas the efficiency increases if $r_{ac,ref}$ increases for $r_{ac} < \sqrt{1 + m_{av}}$. Based on (22.b), the joint achievement of inverter saturation prevention and maximum efficiency is guaranteed if inequality (25) is verified:

$$v_{in}\, n_{i\,\max} - 1 \ge \frac{m_{pk}}{1 + \sqrt{1 + m_{av}}} \tag{25}$$

Equations (22)-(25) allow achieving a well predictable operating condition, providing a trade-off between the charge delivered to the battery and the resulting energy efficiency, by optimizing the control setup. In fact, if (25) is fulfilled, we have the maximum efficiency at the boundary of the inverter duty-cycle saturation. Accordingly, the resulting inverter and post-regulator control references, given in (26), provide the inverter and post-regulator control set up ensuring WPT-DBC optimal performances:

$$I_{1,ref} = \frac{4V_{in}}{\pi R_1} \frac{n_{i\,\max}\left(1 + \sqrt{1 + m_{av}}\right)}{\left(1 + m_{pk} + \sqrt{1 + m_{av}}\right)} = I_{1,opt} \tag{26.a}$$

$$r_{ac,ref} = \sqrt{1 + m_{av}} = r_{ac,opt} \tag{26.b}$$

It cannot be excluded that accepting the occurrence of the inverter duty-cycle saturation may provide some advantage in terms of increased charge or increased efficiency, if compared to the non-saturating inverter duty-cycle operation. However, the assessment of this eventuality is not easy to be analytically done, due to the integrals Γ_{m1} and Γ_{m2}. For this analysis, numerical computations are required, as it will be shown in Section IV.

B. MUTUAL INDUCTANCE OPTIMIZATION

Let us now consider the problem 2), by defining a criterion to determine the optimal values of m_{pk} and m_{av} ensuring the desired efficiency and charge performances. In particular, if we assume non-saturating inverter duty-cycle operation, then we can analyze the battery charge and the energy efficiency when $r_{ac,ref} = r_{ac,opt}$ and $I_{1,ref} = I_{1,opt}$. From (23) and (24) we get:

$$Q_{dc} = Q_0 \frac{m_{av}\sqrt{1 + m_{av}}}{\left(1 + m_{pk} + \sqrt{1 + m_{av}}\right)^2},$$
$$Q_0 = \frac{8V_{in}^2 n_{i\,\max}^2}{\pi^2 R_1} \frac{\Delta t}{V_{dc}} \tag{27}$$

$$\eta = \frac{m_{av}}{\left(1 + \sqrt{1 + m_{av}}\right)^2} \tag{28}$$

Let us assume $m_{pk} = K m_{av}$, with $K > 1$. Then, (27) and (28) highlight that increasing m_{av} reduces the charge and increases the efficiency, while increasing m_{pk} reduces the charge. Therefore, some other elements are needed to identify the best combination of m_{pk} and m_{av} values.

A desirable goal is to limit the winding losses, especially in the RX coil. In fact, as the RX coil is on board the vehicle, it must be as small as possible and as light as possible. The size and weight of the RX coil are determined by the winding, the casing and the heatsink, which can be quite large and heavy, if the RX coil power dissipation is high. Let us then consider the TX and RX coils dissipation when $r_{ac,ref} = r_{ac,opt}$ and $I_{1,ref} = I_{1,opt}$. Under these conditions, the active power dissipated by the TX coil is constant during the time interval Δt. Based on (2.a), the average power dissipated by the TX coil is given by (29):

$$P_{R_1} = P_0 \frac{\left(1 + \sqrt{1 + m_{av}}\right)^2}{\left(1 + m_{pk} + \sqrt{1 + m_{av}}\right)^2},$$
$$P_0 = \frac{8V_{in}^2 n_{i\,\max}^2}{\pi^2 R_1} \tag{29}$$

The active power dissipated by the RX coil, instead, is not constant during the time interval Δt. Therefore, we must calculate the average value of the active power over this interval based on (2.b), thus obtaining (30):

$$P_{R_2} = \frac{1}{\Delta t}\int_{t_0}^{t_1} p_{R_2}(t)dt = P_0 \frac{m_{av}}{\left(1 + m_{pk} + \sqrt{1+m_{av}}\right)^2} \quad (30)$$

Equations (28), (29) and (30) provide the bases for the coil pair design, oriented at identifying the combination of m_{pk} and m_{av} allowing to:

a) keep the RX coil power losses under a given value;
b) ensure an efficiency above a given value;
c) provide a charge above a given value.

If the RX coil power loss target is a given value $P_{R2\max}$, as suggested by goal *a*), then from (30), we must fulfill the condition (31):

$$m_{pk}^2 + 2\left(1+\sqrt{1+m_{av}}\right)m_{pk} + m_{av}\left(\frac{\rho-1}{\rho}\right) + 2\left(1+\sqrt{1+m_{av}}\right) > 0 \quad (31)$$

where $\rho = P_{R2\max}/P_0$. Solving (31) with respect to m_{pk} yields (32):

$$m_{pk} > -\left(1+\sqrt{1+m_{av}}\right) + \sqrt{\frac{m_{av}}{\rho}} = m_{pk\,\min} \quad (32)$$

If the efficiency target is a given value η, as suggested by goal *b*), then from (28) m_{av} must fulfill the condition (33):

$$\frac{m_{av}}{\left(1+\sqrt{1+m_{av}}\right)^2} > \eta \quad (33)$$

Solving (33) with respect to m_{av} yields (34):

$$m_{av} > m_{av\,\min} = \frac{4\eta}{(\eta-1)^2} \quad (34)$$

Finally, if the charge target requires a minimum threshold $Q_{dc\min}$, as suggested by goal *c*), then from (27) the vehicle speed must fulfill the condition (35):

$$v < v_{\max} = v_0 \frac{m_{av}\sqrt{1+m_{av}}}{\left(1+m_{pk}+\sqrt{1+m_{av}}\right)^2}, \qquad v_0 = \frac{P_0 L}{V_{dc} Q_{dc\,\min}} \quad (35)$$

where $v = L/\Delta t$ is the constant speed of the vehicle, covering the distance L between the start and end points of the trajectory.

C. OVERALL SYSTEM OPTIMIZATION

Based on the equations discussed in the previous two subsections, given the input voltage V_{in}, the output voltage V_{dc}, the TX coil resistance R_1, a procedure for optimal RX coil design can be formulated as follows:

step#1. calculate the minimum average value $m_{av\min}$ using (34), based on the required minimum energy efficiency η;

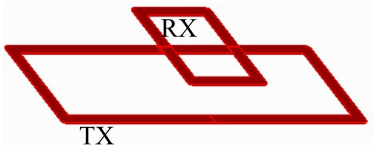

TX wire cross-section = 28 mm²
TX number of turns = 10
TX inner dimensions = 1.5m x 0.5m

RX wire cross-section = 28 mm²
RX number of turns = 10
RX inner dimensions = 0.3m x 0.5m

FIGURE 3. Case study: TX and RX coils.

step#2. calculate the minimum peak value $m_{pk\min}$ using (32), based on the maximum RX coil power dissipation $P_{R2\max}$;
step#3. select m_{av} and m_{pk} just above $m_{av\min}$ and $m_{pk\min}$;
step#4. evaluate the maximum vehicle speed $v_{\max}$ using (35), based on the required minimum charge $Q_{dc\min}$;
step#5. optimize the control based on (26);
step#6. design the RX coil so that the mutual inductance M and resistance R_2 fulfill the reference values of m_{pk} and m_{av}.

In *step#3*, m_{av} and m_{pk} must be as close as possible to $m_{av\min}$ and $m_{pk\min}$ to allow higher vehicle speed according to (35).

IV. CASE STUDIES

A. SYSTEM ANALYSIS

The WPT charger configuration and operating conditions adopted for our case study are referred to a real SS-WPT-DBC investigated in the frame of the European H2020-EMPIR MICEV project [30] and [31], characterized by the values of the parameters listed in Table 1. The details of inverter and post-regulator implementation are described in [25]. The coil pair of this WPT-DBC is shown in Fig. 3. Under low-speed conditions and in case of no lateral displacement, it has been proved that the analytical behavioral model of the mutual inductance of this coil pair is given by (36), as discussed in detail in [32], [33]:

$$M(x_t,\ y_t = 0) = p_0 \tanh\left[p_1(x_t^2 + p_2)\right] + p_3 \tan^{-1}(|p_4 x_t|^{p_5}) + p_6 \quad (36)$$

where M is the mutual inductance in μH, x_t and y_t are the longitudinal and lateral displacements between the center of the RX and TX coil at the time instant t, in meters, and the coefficients $p_0, \ldots, p_6$ are listed in Table 2. The RX coil is assumed placed 20 cm above the TX coil.

According to (36), Fig. 4 (a) shows the plot of the normalized squared mutual inductance factor m while the vehicle is moving (vehicle speed of 4 km/h) along the trajectory corresponding to the longitudinal symmetry axis of the TX coil, represented by the black arrow in Fig. 4(b).

From (36), we can evaluate the peak value of the normalized squared mutual inductance for xt=0, as given in (37):

$$m_{pk} = \frac{\omega_o^2 M_0^2}{R_1 R_2} = \frac{\omega_o^2}{R_1 R_2}\left[p_0 \tanh(p_1 p_2) + p_3 \frac{\pi}{2} + p_6\right]^2 \quad (37)$$

where M_0 is the value of the mutual inductance when the centers of TX and RX coils are perfectly aligned. From (37),

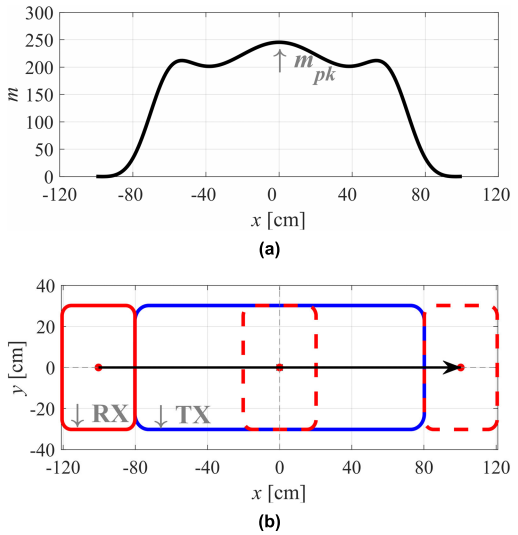

FIGURE 4. (a) Plot of the *m* for the nominal trajectory of the RX coil moving along the longitudinal axis of the TX coil (no lateral displacement). (b) Nominal trajectory of the RX coil (red rectangle) over one TX coil (blue rectangle).

TABLE 1. Case study: WPT-DBC parameters.

Quantity	Unit	Value
V_{in}	[V]	500
V_{dc}	[V]	370
ω_o	[krad/s]	534
$I_{1,ref}$	[A]	40
$I_{2,\mathrm{rms}}$	[A]	50
R_1	[Ω]	0.78
L_1	[H]	281.4
R_2	[Ω]	0.53
L_2	[H]	119.8

TABLE 2. Coefficients of model (36) for the given RX coil.

p_0	p_1	p_2	p_3	p_4	p_5	p_6
-30.3265	2.7423	-0.4289	-23.3234	-1.6378	-3.9922	30.4410

based on coefficients shown in Table 2, we have m_{pk} =245 and m_{av} =154. From (22.a), we get D_0 =0.03. Accordingly, we adopt D_{imin} = 0.02 to prevent the inverter duty-cycle saturation to D_{imin}. Moreover, to fully optimize the inverter and the post-regulator control setup, from (26) we get $I_{1,opt}$ = 42.4 A and $r_{ac,opt}$ = 12.5. With a vehicle speed of 4 km/h, based on (29)(30) the resulting average power P_{R1} and P_{R2} dissipated by the TX and RX coil are about 700 W and 600 W, respectively. Based on (27), the charge delivered to the battery is 36.6 C.

Let us now analyze the impact of the control setup. The WPT-DBC model based on (10)(14)(15)(17)(20)(21) has been implemented and solved numerically in MATLAB. Figures 5 and 6 show the plots of the inverter and post-regulator duty-cycles, the DC input and DC output currents, the charge delivered to the battery, and the input and output energy, for different values of $r_{ac,ref}$. In particular, we consider a series of values symmetrical with respect to $r_{ac,opt}$:

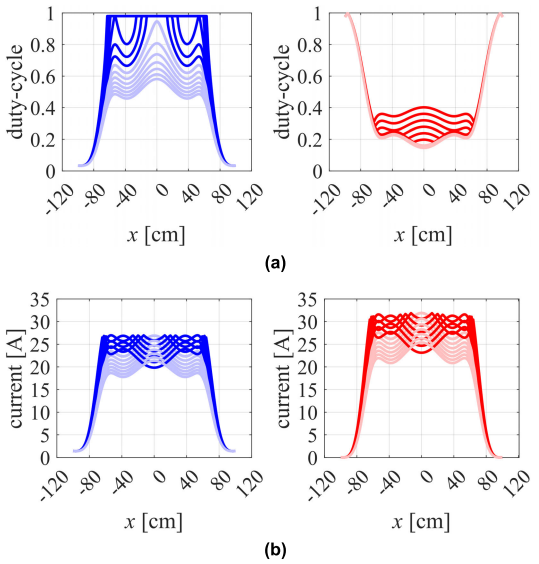

FIGURE 5. (a) Inverter duty-cycle (blue) and post-regulator duty-cycle (red) for $r_{ac,ref} = r_{ac,opt}(1\text{-}\varepsilon)$ (dark color) and $r_{ac,ref} = r_{ac,opt}(1+\varepsilon)$ (light color). (b) Inverter input current (blue) and post-regulator output current (red) for $r_{ac,ref} = r_{ac,opt}(1\text{-}\varepsilon)$ (dark color) and $r_{ac,ref} = r_{ac,opt}(1+\varepsilon)$ (light color).

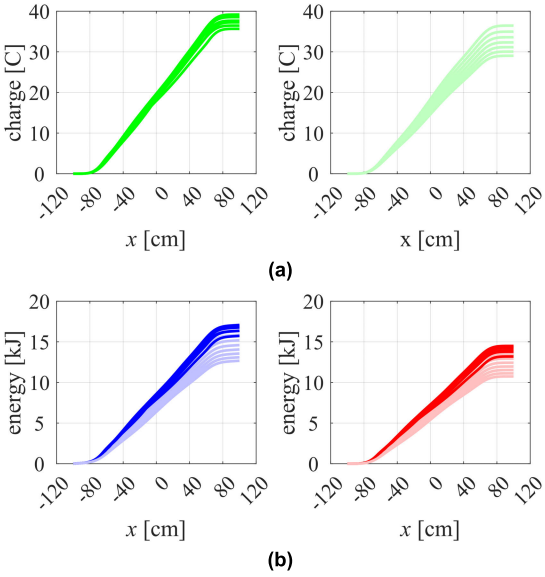

FIGURE 6. Charge transferred to the battery for $r_{ac,ref} = r_{ac,opt}(1\text{-}\varepsilon)$ (dark color) and $r_{ac,ref} = r_{ac,opt}(1+\varepsilon)$ (light color). (b) Input energy (blue) and battery delivered energy (red) for $r_{ac,ref} = r_{ac,opt}(1\text{-}\varepsilon)$ (dark color) and $r_{ac,ref} = r_{ac,opt}(1+\varepsilon)$ (light color).

namely, $r_{ac,opt}(1\text{-}\varepsilon)$ and $r_{ac,opt}(1+\varepsilon)$, with $\varepsilon = \{0.00, 0.05, 0.10, 0.15, 0.20, 0.25, 0.30\}$. The curves with dark colors correspond to the series of lower values $r_{ac,ref} = r_{ac,opt}(1\text{-}\varepsilon)$, for which the inverter duty-cycle saturates to D_{imax}, whereas the curves with light colors correspond to the series of upper values $r_{ac,ref} = r_{ac,opt}(1+\varepsilon)$, for which the inverter never saturates.

The resulting values of the total input and output charges and of the energy efficiency for each value of ε are plotted in Fig. 7, showing that the charge delivered to the battery is maximum for $r_{ac,ref}$ = 0.85 $r_{ac,opt}$ = 10.6, whereas

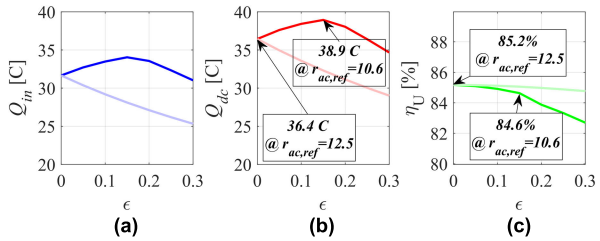

FIGURE 7. (a) Input charge, (b) output charge, (c) energy efficiency, for $r_{ac,ref} = r_{ac,opt}(1\text{-}\varepsilon)$ (dark color) and $r_{ac,ref} = r_{ac,opt}(1+\varepsilon)$ (light color).

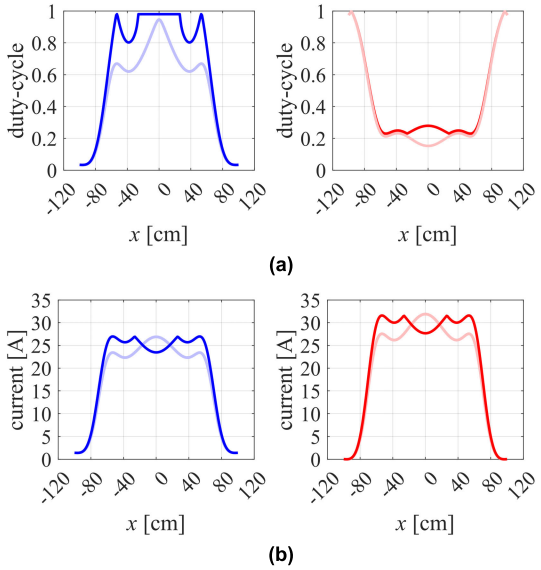

FIGURE 8. (a) Inverter duty-cycle (blue) and post-regulator duty-cycle (red) for $r_{ac,ref} = 0.85\, r_{ac,opt}$ (dark color) and $r_{ac,ref} = r_{ac,opt}$ (light color). (b) Input dc current I_{in} (blue) and output dc current I_{dc} (red) for $r_{ac,ref} = 0.85\, r_{ac,opt}$ (dark color) and $r_{ac,ref} = r_{ac,opt}$ (light color).

the maximum efficiency is reached for $r_{ac,ref} = r_{ac,opt} = 12.5$. From Fig. 7(b) and Fig. 7(c), the charge and the efficiency for $r_{ac,ref} = 10.6$ are respectively $+6.9\%$ higher and -0.7% lower than the charge and the efficiency for $r_{ac,ref} = r_{ac,opt}$.

The plots of Fig. 8 compare the inverter and post-regulator duty-cycles and the inverter input current and the post-regulator output current for $r_{ac,ref} = r_{ac,opt}$ and $r_{ac,ref} = 0.85\, r_{ac,opt}$. These numerical results show there can be an incremental charge benefit while accepting inverter duty-cycle saturation to D_{imax}, with almost negligible efficiency degradation. Unfortunately, the optimal $r_{ac,ref}$ setting ensuring the inverter duty-cycle saturation and the maximum charge increase, is not analytically predictable.

The predictions of WPT-DBC operation based on the model previously implemented in MATLAB have been further validated by means of PSIM numerical simulations, based on the schematic shown in Fig. 9. The instant value of M is generated by a C-block that calculates the mutual inductance as a function of the instant position x of the RX coil center, according to (37), given by a generator emulating the constant speed transit of the vehicle. The plots in Fig. 10 show the results of PSIM simulations for $r_{ac,ref} = r_{ac,opt}$. The inverter duty-cycle and current (blue curves) and the

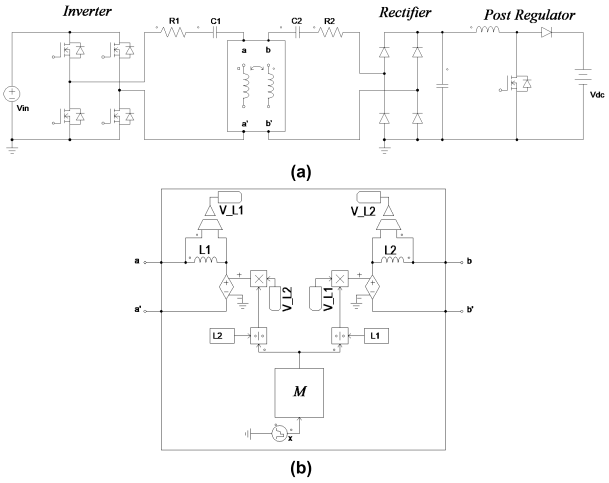

FIGURE 9. PSIM simulation schematic: (a) WPT charger complete schematic and (b) detail of coupled inductor implementation, with the mutual inductance value given by a C-block calculating M as a function of the instant position x of the RX coil center.

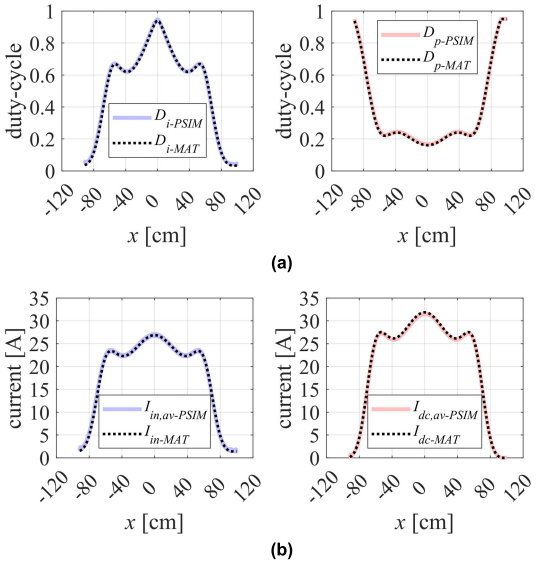

FIGURE 10. PSIM simulation results. (a) Inverter duty-cycle (blue curve) and post-regulator duty-cycle (red curve) for $r_{ac,ref} = r_{ac,opt}$, *versus* MATLAB results (black dotted curves). (b) Inverter current (blue curve) and post-regulator current (red curve) for $r_{ac,ref} = r_{ac,opt}$, *versus* MATLAB results (black dotted curves).

post-regulator duty-cycle and current (red curve) have been compared to the corresponding theoretical predictions (black dotted curves), obtained by implementing the model previously discussed in a MATLAB routine. The PSIM simulations results clearly confirm the MATLAB theoretical model.

B. SYSTEM DESIGN

The purpose of this second case study is to discuss the system-level performance optimization. The physical design of the RX coil given the desired values of m_{av} and m_{pk} is not the goal of this case study analysis. Nevertheless, it is worth to point out that a moderate change of the m_{av} and m_{pk} values can be practically achieved by accommodating different ferrite pads on the TX and RX coils without changing the coil pair windings.

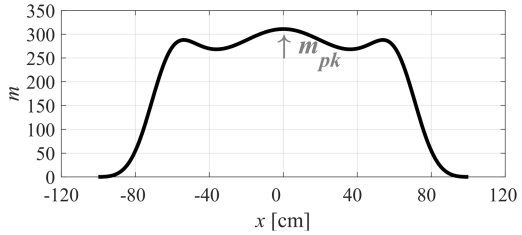

FIGURE 11. Shape of m for the modified RX coil, which moves along the longitudinal axis of the TX coil.

TABLE 3. Coefficients of model (36) for the new RX coil.

p_0	p_1	p_2	p_3	p_4	p_5	p_6
-31.219	2.742	-0.449	-23.323	-1.638	-3.992	31.555

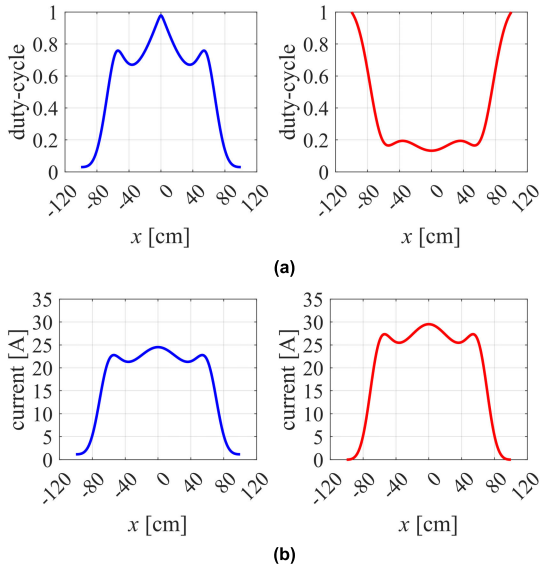

FIGURE 12. (a) Inverter duty-cycle (blue) and post-regulator duty-cycle (red) for $r_{ac,opt} = 14.4$ and $I_{1,opt} = 38.5$ A. (b) Inverter input current (blue) and post-regulator output current (red) for $r_{ac,opt} = 14.4$ and $I_{1,opt} = 38.5$ A.

Let us suppose that our target is to achieve $\eta_{\min} = 87\%$, $Q_{dc\min} = 50$ C and $P_{R2\max} = 500$ W, over a distance $L = 2$ m. From (32), (34) and (35), we get $m_{av\min} = 206$, $m_{pk\min} = 311$, and $v_{\max} = 0.7862$ m/s ($\cong 2.83$ km/h), respectively. The RX coil must be modified to achieve the new values of $m_{av} \geq m_{av\min}$ and $m_{pk} \geq m_{pk\min}$. Accordingly, the coefficients $p_0, \ldots, p_6$ listed in Table 3 have been adopted, which refer to an RX coil ensuring $m_{av} = 207$ and $m_{pk} = 311$. The vehicle speed has been fixed 2.8 km/h.

Fig. 11 shows the modified shape of m along the nominal trajectory of the RX coil over the TX coil. By using these values of m_{av} and m_{pk}, from (26) we get $I_{1,opt} = 38.5$ A and $r_{ac,opt} = 14.4$.

The plots of Fig. 12 provide the MATLAB results of the inverter and post-regulator duty-cycle values, and of the input and output current for the given values of $r_{ac,opt}$ and $I_{1,opt}$. Finally, the plots of Fig. 13 show the input and

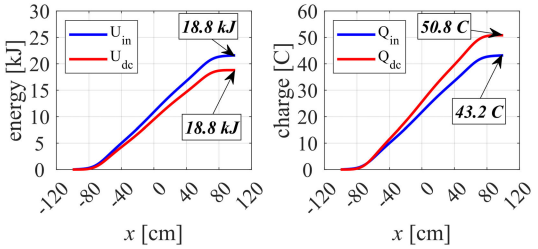

FIGURE 13. Left-side: input energy (blue) and battery delivered energy (red). Right-side: input charge (blue) and charge transferred to the battery (red) for $r_{ac,opt} = 14.4$ and $I_{1,opt} = 38.5$ A.

output energy and charge, thus confirming that the minimum required charge ($Q_{dc} = 50.8$ C $> Q_{dc\min}$) and the minimum required efficiency ($\eta = 87\%$) have been achieved.

V. CONCLUSION

A system-level approach is required to match the control parameters with the coil pair characteristics, in order to fulfill the efficiency, power dissipation and charge requirements of a Wireless Power Transfer Dynamic Battery Charger (WPT-DBC) for electric vehicles. To this purpose, a novel dimensionless model and a design method have been presented in this paper, providing guidelines for optimal inverter and post-regulator controls setup in a series-series WPT-DBC. The analysis and design equations presented in the paper are scalable, since they are derived for dimensionless setup factors, physical parameters and performance metrics. The architecture of power converters and relevant control of a real series-series WPT-DBC prototype, previously discussed in the literature, have been considered to validate the theoretical predictions provided by the method presented in the paper.

REFERENCES

[1] A. Ahmad, M. S. Alam, and R. Chabaan, "A comprehensive review of wireless charging technologies for electric vehicles," *IEEE Trans. Transport. Electrific.*, vol. 4, no. 1, pp. 38–63, Mar. 2018.
[2] S. Laporte, G. Coquery, V. Deniau, A. De Bernardinis, and N. Hautière, "Dynamic wireless power transfer charging infrastructure for future EVs: From experimental track to real circulated roads demonstrations," *World Electr. Veh. J.*, vol. 10, no. 4, p. 84, Nov. 2019.
[3] D. Patil, M. K. McDonough, J. M. Miller, B. Fahimi, and P. T. Balsara, "Wireless power transfer for vehicular applications: Overview and challenges," *IEEE Trans. Transport. Electrific.*, vol. 4, no. 1, pp. 3–37, Mar. 2018.
[4] A. C. Bagchi, A. Kamineni, R. A. Zane, and R. Carlson, "Review and comparative analysis of topologies and control methods in dynamic wireless charging of electric vehicles," *IEEE J. Emerg. Sel. Topics Power Electron.*, vol. 9, no. 4, pp. 4947–4962, Aug. 2021.
[5] *Wireless Charging of Electric and Plug-In Hybrid Vehicles*, Standard J2954, Society of Automotive Engineers. Accessed: Nov. 15, 2021. [Online]. Available: https://www.sae.org/standards/content/j2954_202010/
[6] *Electric Vehicle Wireless Power Transfer (WPT) Systems—Part 1: General Requirements*, Standard IEC 61980-1:2015, 2015. [Online]. Available: https://webstore.iec.ch/publication/22951
[7] W. Zhang and C. C. Mi, "Compensation topologies of high-power wireless power transfer systems," *IEEE Trans. Veh. Technol.*, vol. 65, no. 6, pp. 4768–4778, Jun. 2016.
[8] S. Jayalath and A. Khan, "Design, challenges, and trends of inductive power transfer couplers for electric vehicles: A review," *IEEE J. Emerg. Sel. Topics Power Electron.*, vol. 9, no. 5, pp. 6196–6218, Oct. 2021.

[9] W. Zhang, J. C. White, A. M. Abraham, and C. C. Mi, "Loosely coupled transformer structure and interoperability study for EV wireless charging systems," *IEEE Trans. Power Electron.*, vol. 30, no. 11, pp. 6356–6367, Nov. 2015.
[10] H. Kim *et al.*, "Coil design and measurements of automotive magnetic resonant wireless charging system for high-efficiency and low magnetic field leakage," *IEEE Trans. Microw. Theory Techn.*, vol. 64, no. 2, pp. 383–400, Feb. 2016.
[11] J. Deng, W. Li, T. D. Nguyen, S. Li, and C. C. Mi, "Compact and efficient bipolar coupler for wireless power chargers: Design and analysis," *IEEE Trans. Power Electron.*, vol. 30, no. 11, pp. 6130–6140, Nov. 2015.
[12] X. Mou, O. Groling, A. Gallant, and H. Sun, "Energy efficient and adaptive design for wireless power transfer in electric vehicles," in *Proc. IEEE 83rd Veh. Technol. Conf. (VTC Spring)*, May 2016, pp. 1–5.
[13] R. Bosshard, U. Iruretagoyena, and J. W. Kolar, "Comprehensive evaluation of rectangular and double-D coil geometry for 50 kW/85 kHz IPT system," *IEEE J. Emerg. Sel. Topics Power Electron.*, vol. 4, no. 4, pp. 1406–1415, Dec. 2016.
[14] A. Hariri, A. Elsayed, and O. A. Mohammed, "An integrated characterization model and multiobjective optimization for the design of an EV charger's circular wireless power transfer pads," *IEEE Trans. Magn.*, vol. 53, no. 6, pp. 1–4, Jun. 2017.
[15] Y. Liu, R. Mai, D. Liu, Y. Li, and Z. He, "Efficiency optimization for wireless dynamic charging system with overlapped DD coil arrays," *IEEE Trans. Power Electron.*, vol. 33, no. 4, pp. 2832–2846, Apr. 2018.
[16] I. U. Castillo-Zamora, P. S. Huynh, D. Vincent, F. J. Perez-Pinal, M. A. Rodriguez-Licea, and S. S. Williamson, "Hexagonal geometry coil for a WPT high-power fast charging application," *IEEE Trans. Transport. Electrific.*, vol. 5, no. 4, pp. 946–956, Dec. 2019.
[17] B.-G. Choi and Y.-S. Kim, "New structure design of ferrite cores for wireless electric vehicle charging by machine learning," *IEEE Trans. Ind. Electron.*, vol. 68, no. 12, pp. 12162–12172, Dec. 2021.
[18] Z. Luo, X. Wei, M. G. S. Pearce, and G. A. Covic, "Multiobjective optimization of inductive power transfer double-D pads for electric vehicles," *IEEE Trans. Power Electron.*, vol. 36, no. 5, pp. 5135–5146, May 2021.
[19] A. Azad, A. Echols, V. Kulyukin, R. Zane, and Z. Pantic, "Analysis, optimization, and demonstration of a vehicular detection system intended for dynamic wireless charging applications," *IEEE Trans. Transport. Electrific.*, vol. 5, no. 1, pp. 147–161, Mar. 2019.
[20] C. Park, S. Lee, S. Y. Jeong, G.-H. Cho, and C. T. Rim, "Uniform power I-type inductive power transfer system with *DQ*-power supply rails for on-line electric vehicles," *IEEE Trans. Power Electron.*, vol. 30, no. 11, pp. 6446–6455, Nov. 2015.
[21] J. M. Miller, O. C. Onar, and M. Chinthavali, "Primary-side power flow control of wireless power transfer for electric vehicle charging," *IEEE J. Emerg. Sel. Topics Power Electron.*, vol. 3, no. 1, pp. 147–162, Mar. 2015.
[22] S. Wang, J. Chen, Z. Hu, C. Rong, and M. Liu, "Optimisation design for series-series dynamic WPT system maintaining stable transfer power," *IET Power Electron.*, vol. 10, no. 9, pp. 987–995, Jul. 2017.
[23] T. Diekhans and R. W. D. Doncker, "A dual-side controlled inductive power transfer system optimized for large coupling factor variations and partial load," *IEEE Trans. Power Electron.*, vol. 30, no. 11, pp. 6320–6328, Nov. 2015.
[24] G. Buja, M. Bertoluzzo, and K. N. Mude, "Design and experimentation of WPT charger for electric city car," *IEEE Trans. Ind. Electron.*, vol. 62, no. 12, pp. 7436–7447, Dec. 2015.
[25] R. Ruffo, V. Cirimele, M. Diana, M. Khalilian, A. L. Ganga, and P. Guglielmi, "Sensorless control of the charging process of a dynamic inductive power transfer system with an interleaved nine-phase boost converter," *IEEE Trans. Ind. Electron.*, vol. 65, no. 10, pp. 7630–7639, Oct. 2018.
[26] Q. Zhu, L. Wang, Y. Guo, C. Liao, and F. Li, "Applying LCC compensation network to dynamic wireless EV charging system," *IEEE Trans. Ind. Electron.*, vol. 63, no. 10, pp. 6557–6567, Oct. 2016.
[27] V.-B. Vu, M. Dahidah, V. Pickert, and V.-T. Phan, "A high-power multiphase wireless dynamic charging system with low output power pulsation for electric vehicles," *IEEE J. Emerg. Sel. Topics Power Electron.*, vol. 8, no. 4, pp. 3592–3608, Dec. 2020.
[28] A. Kamineni, G. A. Covic, and J. T. Boys, "Self-tuning power supply for inductive charging," *IEEE Trans. Power Electron.*, vol. 32, no. 5, pp. 3467–3479, May 2017.
[29] N. Femia and G. Di Capua, "Impact of receiver conversion configuration on the efficiency of wireless power transfer systems," in *Proc. 14th Int. Conf. Synth., Modeling, Anal. Simulation Methods Appl. Circuit Design (SMACD)*, Jun. 2017, pp. 1–4.
[30] *Project EU-H2020, MICEV—Metrology for Inductive Charging of Electric Vehicles*. Accessed: Nov. 15, 2021. [Online]. Available: https://www.micev.eu/
[31] M. Zucca, O. Bottauscio, S. Harmon, R. Guilizzoni, F. Schilling, M. Schmidt, P. Ankarson, T. Bergsten, K. Tammi, P. Sainio, and J. B. Romero, "Metrology for inductive charging of electric vehicles (MICEV)," in *Proc. AEIT Int. Conf. Electr. Electron. Technol. Automot. (AEIT AUTOMOTIVE)*, Jul. 2019, pp. 1–6.
[32] K. Stoyka, G. Di Capua, G. Di Mambro, N. Femia, F. Freschi, A. Maffucci, and S. Ventre, "Behavioral models for the analysis of dynamic wireless charging systems for electrical vehicles," in *Proc. IEEE Int. Symp. Circuits Syst. (ISCAS)*, Oct. 2020, pp. 1–5.
[33] G. Di Capua, A. Maffucci, K. Stoyka, G. Di Mambro, S. Ventre, V. Cirimele, F. Freschi, F. Villone, and N. Femia, "Analysis of dynamic wireless power transfer systems based on behavioral modeling of mutual inductance," *Sustainability*, vol. 13, no. 5, p. 2556, Feb. 2021.

GIULIA DI CAPUA (Senior Member, IEEE) received the B.Sc. and M.Sc. degrees (Hons.) in electronic engineering and the Ph.D. degree in information engineering from the University of Salerno, Italy, in 2006, 2009, and 2013, respectively.

From 2013 to 2016 and from 2016 to 2020, she was a Post-Doctoral Researcher and a Research Assistant, respectively, both with the University of Salerno. Since 2021, she has been an Assistant Professor with the Department of Electrical and Informational Engineering, University of Cassino and Southern Lazio, Italy. Her research interests include power management, switching-mode power supplies optimization, magnetic components design, and wireless power transfer systems.

Dr. Di Capua is a member (and currently the Chair-Elect) of the IEEE CASS Power and Energy Circuits and Systems (PECAS) Technical Committee. In 2017, she was the General Chair of the 14th International Conference on Synthesis, Modelling, Analysis and Simulation Methods and Applications to Circuit Design (SMACD 2017). She is the Track Chair on topics inherent to power systems and electronic circuits for flagship conferences of the IEEE Circuits and Systems Society (CASS). She is an Associate Editor of IEEE TRANSACTIONS ON CIRCUITS AND SYSTEMS—I: REGULAR PAPERS (IEEE TCAS-I).

NICOLA FEMIA (Senior Member, IEEE) received the Laurea degree (Hons.) in industrial technologies engineering from the University of Salerno, Italy, in 1988.

He was an Assistant Professor, from 1990 to 1998, was an Associate Professor, from 1998 to 2001, and has been a Full Professor of electrotechnics at the University of Salerno, since 2001, where he teaches power electronics in the electronic engineering master's program. He leads the Power Electronics and Renewable Sources Laboratory, Department of Information and Electrical Engineering and Applied Mathematics, University of Salerno. In 2014, he was a Visiting Professor with the Electrical Engineering Department, Stanford University, Stanford, CA, USA, where he taught power electronics control and energy aware design in the electrical engineering enhanced master's program. In the last two decades, he has directed and developed tens of research and education projects on power electronics topics, in collaboration with worldwide leader electronic companies. He held more than 50 invited lectures, courses, and seminars on power electronics design and education for universities and industries over Europe, USA, China, and India. He co-authored more than 200 scientific papers, one book, and seven patents. His research interests include circuit theory and applications, design, and optimization of switching power supplies, magnetic power components modeling and optimization, power electronics and control techniques for photovoltaic systems, and wireless power transfer systems.

Prof. Femia was a member of the Administration Council of the University of Salerno, from 2002 to 2005. He was also a member, and the Chairperson from 2009 to 2010, of the Patents Council of the University of Salerno. He has been an Associate Editor of IEEE TRANSACTIONS ON POWER ELECTRONICS, from 1995 to 2003.